Mission Profile Based Reliability Evaluation of Capacitor Banks in Wind Power Converters

Dao Zhou, *Senior Member, IEEE*, Yipeng Song, *Member, IEEE*, Yang Liu, *Senior Member, IEEE*, and Frede Blaabjerg, *Fellow, IEEE*

***Abstract*—With the increasing penetration of wind power, reliable and cost-effective wind energy production is of more and more importance. The doubly-fed-induction-generator-based turbine system is widely used and dominates the wind market. In this paper, an analytical approach to assess reliability for power capacitors, both the dc-link capacitor bank and ac-side filter capacitor bank, is presented considering the annual mission profile. Based on the electrical behavior at various loading conditions, the lifecycle of the single power capacitor can be predicted through its electrothermal stresses. This percentile lifetime can be translated to the Weibull lifetime distribution of the power capacitor by considering the parameter uncertainties and tolerance variations. Thereafter, a reliability block diagram is used to bridge the reliability curves from the component-level of the individual capacitor to the system-level of the capacitor bank. A case study of a 2-MW wind turbine shows that the lifecycle is significantly reduced from the individual capacitor to the capacitor bank, where the dc-link capacitor bank dominates the lifetime consumption. Furthermore, the electrical stresses of the power capacitors are experimentally verified at a down-scaled 7.5 kW prototype.**

***Index Terms*—Aluminum electrolytic capacitor (Al-CAP), doubly-fed induction generator (DFIG), metalized polypropylene film capacitor (MPF-CAP), reliability evaluation.**

I. Introduction

With the increasing penetration of wind power during recent decades, reliable and cost-effective wind energy production is of more and more importance [1]–[3]. In order to reduce the cost of the wind power generation, the power rating of the individual wind turbine is today up-scaled to 8 MW and even above is being prototyped. However, the feedback of the wind turbine market indicates that the best seller is still the turbines rated around 2–3 MW, in which the doubly-fed induction generator (DFIG) is normally employed together with partial-scale power electronic converter [4]. Another tendency of the wind power development is the popularity of offshore wind farms,

Manuscript received March 26, 2018; revised June 18, 2018; accepted July 31, 2018. Date of publication August 14, 2018; date of current version March 29, 2019. This work was supported by the Innovation Fund Denmark through the Advanced Power Electronic Technology and Tools Project. Recommended for publication by Associate Editor T. M. Lebey. *(Corresponding author: Dao Zhou.)*

D. Zhou, Y. Song, and F. Blaabjerg are with the Department of Energy Technology, Aalborg University, Aalborg 9220, Denmark (e-mail:

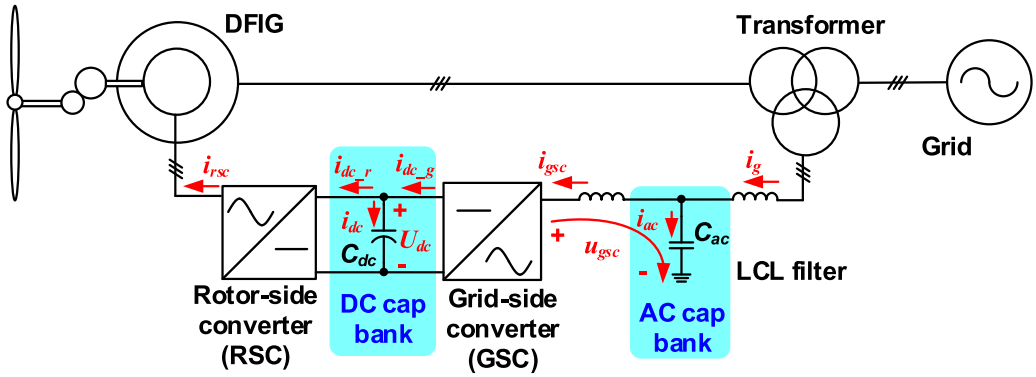

Fig. 1. DC and ac capacitor banks located in a DFIG-based wind turbine system.

reflected by using this model [20]–[22]. In addition, manufacturers present only part of the reliability data, the corresponding lifetime calculation is actually the B_{10} or B_1 lifetime, which means 10% or 1% of the whole samples fail if the operation hours reach the aforementioned lifecycle. In the filed application, as several capacitors are linked in series or in parallel, this component-level B_x lifetime of the single capacitor cannot directly be translated to the system-level B_x lifetime of the capacitor bank.

In this paper, an analytical approach to evaluate the electrical stresses for both the ac-side capacitor and the dc-side capacitor will be presented. Hence, their lifetime can be predicted by considering the long-term mission profile that integrates the power loss and thermal modeling. In order to fill in the research gap between the single capacitor and capacitor bank reliability, the Weibull function-based lifetime distribution of the power capacitors can be obtained by taking the parameter variations and tolerance uncertainties into account. Furthermore, the reliability block diagram can be applied to bridge from the component-level to the system-level reliability distribution.

The remaining of this paper is organized as follows. Section II describes the basic design of dc-side and ac-side capacitors. Section III presents the analysis of the capacitor current by using both simulations and experimental validations. On the basis of the loss and thermal modeling of the power capacitor, the mission profile based lifetime estimation of the individual capacitor is addressed in Section IV. Section V investigates and compares the time-to-failure from a single capacitor to the capacitor bank by using the reliability block diagram. The concluding remarks are drawn Section VI.

II. Design of DC-Side and AC-Side Capacitors

The configuration of a 2 MW DFIG wind turbine system is shown in Fig. 1, where the back-to-back power converter is with a partial-scale power rating compared to the generator. The Al-CAP in the DC-link (DC cap bank) serves as the energy storage and power decoupling between the grid-side converter and the rotor-side converter, and the MPF-CAP in the grid-side (AC cap bank) filters out the current ripple introduced by the PWM switching pattern.

TABLE I
Parameters of 2 MW and 7.5-kW DFIG Systems

Rated power	2 MW	7.5 kW
Operational range of rotor speed	1050-1800 rpm	1200-1800 rpm
Rated amplitude of phase voltage	563 V	311 V
Mutual inductance	2.91 mH	79.30 mH
Stator leakage inductance	0.04 mH	3.44 mH
Rotor leakage inductance	0.06 mH	5.16 mH
Ratio of stator winding and rotor winding	0.369	0.336
DC-link voltage	1050 V	650 V
DC-link capacitor	20 mF	600 μF
Grid-side inductor	125 μH	11 mH
Converter-side inductor	125 μH	7 mH
AC-side filter capacitor	300 μF	6.6 μF
Switching frequency	2 kHz	5 kHz

The selection of the dc-link capacitor $C_{\rm dc}$ is based on the balance of the energy exchange during the transient period [23]

$$C_{\rm dc} \geq \frac{T_r \Delta P_{\rm max}}{2U_{\rm dc}\Delta U_{\rm max}} \tag{1}$$

where $\Delta P_{\rm max}$ denotes the maximum variation of the output power, T_r denotes the control response time, which typically is a few modulation periods, $U_{\rm dc}$ denotes the dc-link voltage, and $\Delta U_{\rm max}$ denotes the maximum voltage variation.

The parameters of the 2-MW DFIG system are listed in Table I. In order to achieve a high ride-through capability during a power voltage sag, the capacitance of 20 mF is selected. Due to the limitation of the rated voltage, 72 pieces of 4700 μF/400 V are chosen—four in series and 18 in parallel [19].

The design procedure of the *LCL* filter is well presented in [24], and the capacitance of 300 μF is designed according to 10% of absorbed reactive power at the rated condition. As the delta connection is normally applied in practice, the equivalent 100 μF is applied, which in practice is realized by ten pieces of 10 μF/780 V from a leading capacitor manufacturer [25].

III. Analysis of Capacitor Electrical Stresses

Based on the parameters of the dc-side and ac-side capacitors, different approaches can be applied to analyze their electrical

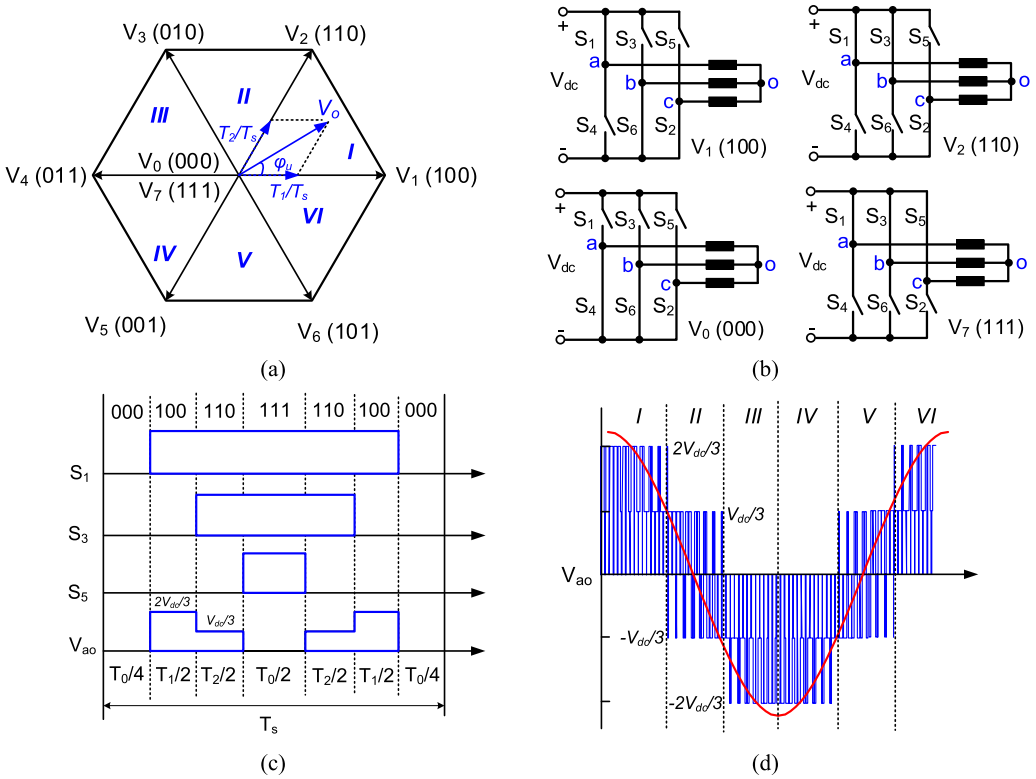

Fig. 2. Illustration of SVM. (a) Six sectors. (b) Switching states existing in Sector I. (c) Phase voltage of converter output in Sector I. (d) Phase voltage of the converter output within a fundamental period.

stresses. Then, the theoretical calculation of the capacitor current can be compared with the simulation under typical loading conditions. The harmonic spectrum of the capacitor current can further be verified by a down-scaled DFIG setup.

A. AC-Side Capacitor Current

In order to evaluate the current flowing through the ac-side filter capacitor, it starts with the output voltage analysis of the grid-side converter. According to the impedance characteristics of the *LCL* filter, both the converter-side current and the grid-side current can thereby be calculated.

For the three-phase system, the space vector modulation (SVM) is preferred compared to the Sinusoidal PWM due to its higher dc-link voltage utilization. The duty cycle of the two adjacent nonzero vectors (d_1, d_2) and the zero vectors (d_0) can be obtained at different sectors

$$\begin{cases} d_1 = \dfrac{\sqrt{3}}{2} M_X \sin\left(\frac{k\pi}{3} - \varphi_u\right) \\ d_2 = \dfrac{\sqrt{3}}{2} M_X \sin\left(\varphi_u - \frac{(k-1)\pi}{3}\right) \\ d_0 = 1 - d_1 - d_2 \end{cases} \tag{2}$$

where k denotes the section number; M denotes the modulation index ($0 \le \mathrm{M} \le 1.15$), which equals the inverter output peak voltage over a half of the dc-link voltage V_{dc}; φ_u denotes the phase angle of the inverter output voltage, and subscript X represents the grid-side converter (GSC).

As shown in Fig. 2(a), six sectors (Sector I to VI) can be divided in accordance with the phase angle of the output voltage φ_u. In the case of Sector I, the voltage vector V_o is generally composed of two adjacent active vectors V_1 (100) and V_2 (110) (with duration periods of T_1 and T_2 within the switching period T_s), as well as two zero vectors V_0 (000) and V_7 (111) (with duration period of T_0 within the switching period T_s). Both the active and zero vectors are symmetrically arranged in order to achieve the minimum harmonics of the output voltage [26]. The possible switching patters of the power devices are described in Fig. 2(b) in details, where active vectors V_1 and V_2, as well as zero vectors V_0 and V_7 are applied. Due to the symmetrical loading of the three-phase system, the phase voltage of the inverter output V_{ao} is illustrated in Fig. 2(c). Depending on various switching states of the power devices, it can be seen that the output voltage includes the levels of $2V_{\mathrm{dc}}/3$, $V_{\mathrm{dc}}/3$, and *0*. By using the similar approach, the voltage waveform of the inverter output can be expected in the cases of other five sectors, which contains three voltage levels within the same sector, as described in Fig. 2(d).

In order to obtain the fundamental and harmonic components of the converter output voltage, the Fourier analysis is necessary to be employed. On the basis of the impedance characteristics of the *LCL* filter, the electrical stresses of the filter capacitor can be calculated. For a pulse voltage, its Fourier coefficient can be calculated by its starting and ending time instants together with its voltage amplitude [26]. Since seven pulse voltages exist within a switching period, as shown in Fig. 2(c), the Fourier coefficient can be summed up together with the duty cycle as calculated in (2) and its corresponding voltage amplitude. With the voltage amplitude distribution in various sectors, as shown in Fig. 2(d), the Fourier coefficient can be further accumulated

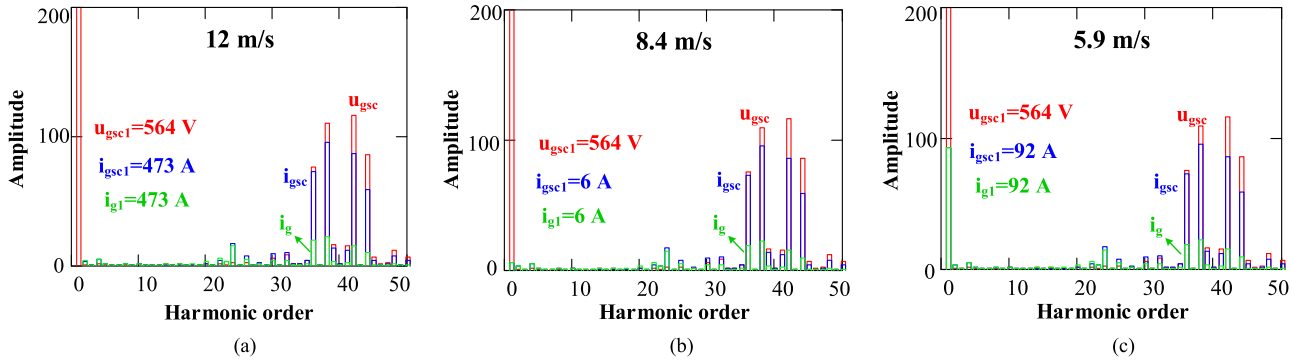

Fig. 3. Voltage and current FFT analysis of the GSC. (a) Super-synchronous mode at the wind speed of 12 m/s. (b) Synchronous mode at the wind speed of 8.4 m/s. (c) Subsynchronous mode at the wind speed of 5.9 m/s. It is noted that $u_{\rm gsc}$ and $u_{\rm gsc1}$ denote the converter voltage and its fundamental component; $i_{\rm gsc}$ and $i_{\rm gsc1}$ denote the converter-side current and its fundamental component; i_g and i_{g1} denote the grid-side current and its fundamental component, all of which are consistent with Fig. 1.

from a single switching period to the whole fundamental period. Thereafter, the fundamental and harmonic components of the converter output voltage can be deduced.

As described in [7], the modulation index and the phase angle of the converter voltage can be deduced based on the GSC modeling represented in the dq-reference frame. The fast Fourier transform (FFT) analysis of the converter voltage is shown in Fig. 3, where the wind speeds of 12, 8.4, and 5.9 m/s represent the super-synchronous, synchronous, and subsynchronous operation of the DFIG. It can be observed that, regardless of the operation modes, the fundamental voltage is always 564 V, which is similar to the grid voltage due to the negligible voltage drop across the *LCL* filter. However, the fundamental component of the converter-side current changes considerably at various wind speeds, which becomes the lowest at the synchronous mode due to little active power flowing through the back-to-back power converter. As the *LCL* filter generally behaves as the low-pass filter, the fundamental component of the grid-side current is exactly the same as the converter-side current. In respect to harmonic components, the voltage harmonic is mainly dominated by harmonic orders around the switching frequency of 2 kHz. As the converter-side current can be achieved with the impedance of the *LCL* filter, it is noted that the dominant harmonics are the same with the voltage harmonics. Due to the resonance frequency of the *LCL* filter at 1162 Hz, the 23rd current harmonic is significantly amplified. Furthermore, since the impedance of the filter capacitor is much less than the grid-side inductor, the switching harmonics are considerably reduced for the grid-side current.

It is well known that the RMS of the voltage or current is defined as the square root of the mean square, which consists of both the fundamental component and harmonic components. In addition, as the output power of the wind turbine obeys an maximum power point tracking (MPPT) algorithm [7], [27], the relationship between the GSC voltage and the wind speed can be established. Based on the FFT analysis of the converter voltage and current, their fundamental, harmonics, and RMS values can be calculated and are as shown in Fig. 4 from the cut-in wind speed (4 m/s) until the rated wind speed (12 m/s). As the fundamental component of the converter voltage is dominant by the grid voltage, it always maintains the same regardless of the wind speeds. However, the fundamental components of both the converter-side current and the GSC are tightly related to the produced power flowing through the GSC, they fluctuate with the wind speed due to the various output power and slip values of the induction generator. In addition, it is noted that the fundamental components of the converter-side current and the grid-side current are almost the same. As the modulation index of the GSC varies a little at different wind speeds, the harmonic component of the converter voltage stays the same, which results in the unchanged harmonic components of the converter-side current and the grid-side current. In addition, it is worthwhile to mention that the grid-side current has much less harmonic, as the majority of the switching harmonics flow through the filter capacitor branch.

With the harmonic spectrum of the converter-side current and grid-side current, their total harmonic distortion (THD) can be obtained. As the harmonic component of the capacitor current is dependent on both its amplitude and phase angle, the worst case THD can be roughly estimated by the sum of the converter-side current and the grid-side current [28]. The simulation result of the GSC is shown in Fig. 5, where the harmonic spectrum of the output voltage, converter-side current, grid-side current, and the ac-side capacitor current is investigated. For the converter output voltage, its fundamental component and dominating harmonics are consistent with the theoretical calculations, as shown in Fig. 3(a). Moreover, the fundamental of the converter-side current and grid-side current are almost the same, and the switching harmonics of the grid-side current are considerably reduced compared with the converter-side converter current. In respect to the capacitor current, it mainly contains the switching harmonics, while the fundamental current is reduced a lot. In order to have a fair comparison, the THD of the capacitor current is calculated compared to the fundamental of the grid-side current.

At different loading conditions, the calculated and simulated THD are summarized and compared in Fig. 6. As shown in Fig. 6(a) and (b), at the wind speed of 12 m/s, the calculated fundamental of the converter-side current and the grid-side current is 1.0 pu with their THD of 34% and 8%, respectively. Moreover, it can be seen that the fundamental component of both the simulated converter-side current and the grid-side current is 0.97 pu, and their THD is 36% and 10%. For the capac-

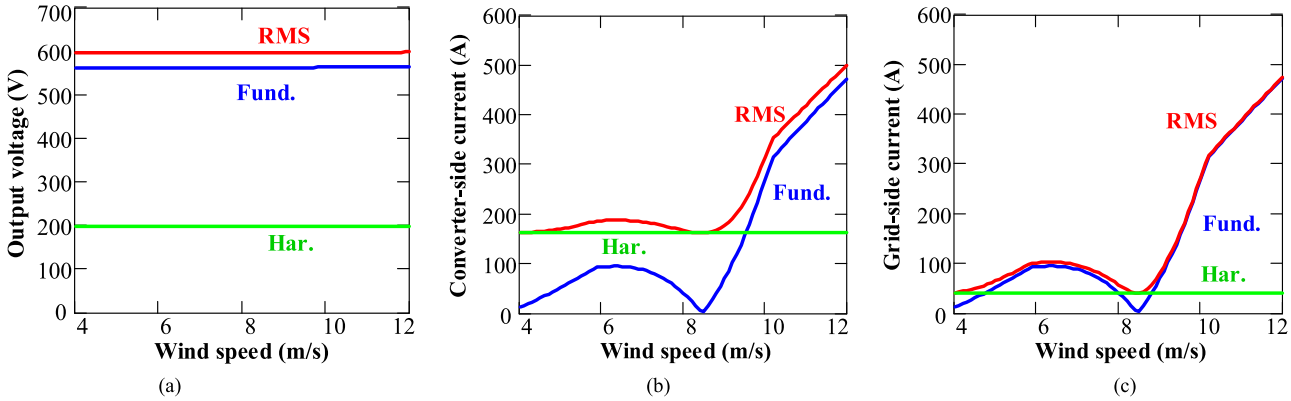

Fig. 4. Analysis of the fundamental, harmonic and RMS components. (a) Converter voltage. (b) Converter-side current. (c) Grid-side current.

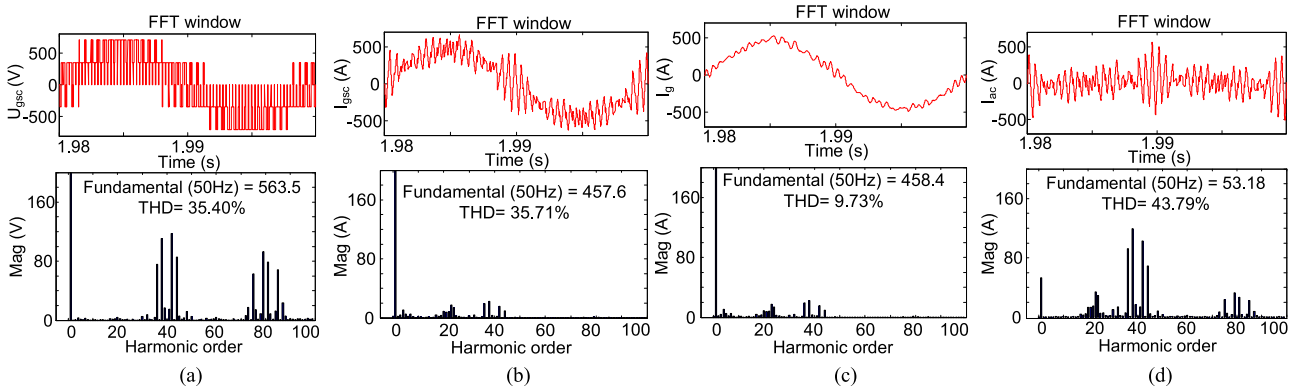

Fig. 5. Simulation results of GSC at the wind speed of 12 m/s in time and frequency domain. (a) Converter output voltage. (b) Converter-side current. (c) Grid-side current. (d) AC-side capacitor current.

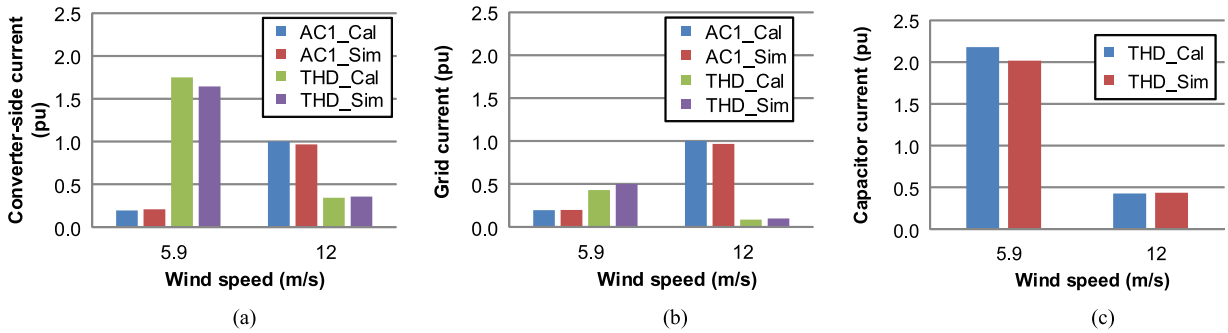

Fig. 6. Harmonic comparison between the calculation (Cal) and simulation (Sim) of ac-side capacitor current. (a) Converter-side current. (b) Grid-side current. (c) Capacitor current.

itor current, the calculated and the simulated THD are 43% and 44%, which agrees well with each other. At the wind speed of 5.9 m/s, it is evident that the fundamental component is considerably reduced due to the lower produced power, while the THD is significantly increased because of the similar harmonic component. Moreover, the THD can be compared with the converter-side current, grid-side current, and capacitor current. It can be seen that the simulation result matches well the theoretical calculation.

B. DC-Side Capacitor Current

Regardless of the GSC and the rotor-side converter (RSC), the relationship between the inverter input and output current obeys Kirchhoff's current law. Neglecting the switching ripple, the three-phase inverter current is purely sinusoidal and respectively delayed $2\pi/3$. The duty cycle of the adjacent nonzero vectors can be calculated with the information of the modulation index and its corresponding voltage phase angle. Owing to the symmetry of the dc-side periodical input current, its average value $I_{\mathrm{dc\_}X\_\mathrm{ave}}$ can be calculated within a half of the switching period [28]

$$I_{\mathrm{dc\_}X\_\mathrm{ave}} = \frac{3}{4} I_X M_X \cos\varphi_X \tag{3}$$

where I denotes the peak value of inverter output current, M denotes the modulation index ($0 \le \mathrm{M} \le 1.15$), φ denotes the phase displacement between the fundamentals of the inverter output voltage and current, and subscript X represents either the

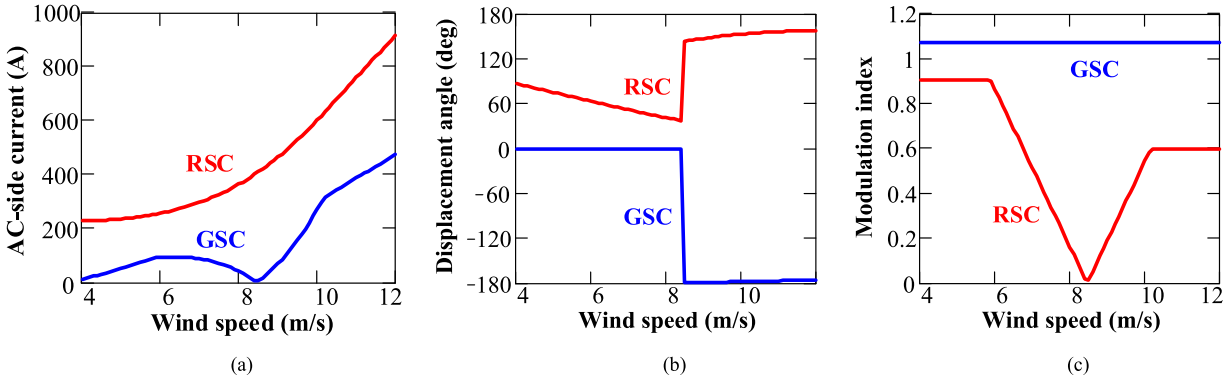

Fig. 7. Operation characteristics of the back-to-back power converters at various wind speeds. (a) AC-side current. (b) Displacement angle. (c) Modulation index. (GSC: grid-side converter; RSC: rotor-side converter.)

GSC or the RSC. Assuming a constant power flow between the inverter ac-side and dc-side, the average inverter input current becomes constant and independent of the output voltage phase angle.

Similarly, the RMS of the inverter current within a switching period can be calculated in a half-switching period. Owing to the symmetries of an ideal three-phase voltage system and the phase-symmetrical structure of the power converter circuit, the analysis can be limited to $\pi/3$-wide interval of the inverter voltage fundamental period [28]

$$I_{dc\_X\_\mathrm{rms}} = I_X \sqrt{\frac{\sqrt{3}}{\pi} M_X \left(\frac{1}{4} + \cos^2 \varphi_X\right)}. \tag{4}$$

On the basis of (3) and (4), the average and RMS values of the dc-side current for both the GSC and the RSC can be obtained. As a consequence, their harmonic of dc-side current can be deduced as

$$I_{\mathrm{dc\_X\_har}} = I_X \sqrt{M_X \left(\frac{\sqrt{3}}{4\pi} + \cos^2 \varphi_X \left(\frac{\sqrt{3}}{\pi} - \frac{9}{16} M_X\right)\right)}. \tag{5}$$

In respect to the dc-link current, it is only related to the harmonic values of the back-to-back power converters due to their same average value of the dc-side current. As a consequence, the worst case THD of the dc-link current can be roughly estimated by the sum of the harmonic components from the GSC and the RSC.

Since the dc-side current of the converter is tightly related to its ac-side current, displacement angle, and the modulation index; Fig. 7 shows their values with the wind speed, where both the GSC and the rotor-side converter are taken into account. For the GSC, it is worth noting that the displacement angle changes from 0° to 180° from the subsynchronous mode to the supersynchronous mode, which indicates the opposite direction of the active power. For the rotor-side converter, the modulation index changes with different wind speeds, and it becomes the lowest at the synchronous mode because of the zero rotor voltage.

According to (3)–(5), the average, RMS, and the harmonic components of the dc-side current can thereby be calculated. As

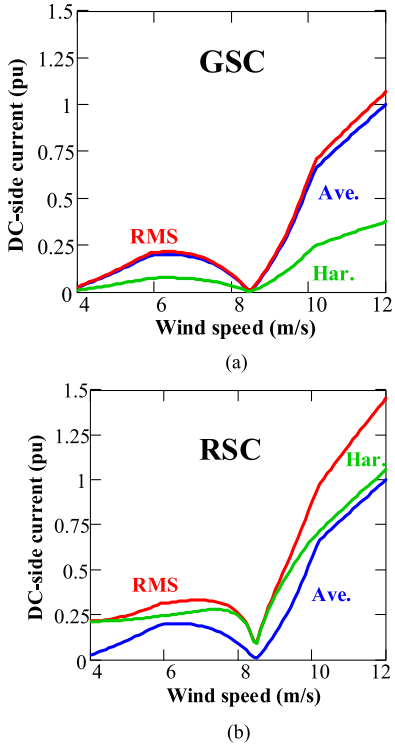

Fig. 8. Analysis of the average, harmonic and RMS values. (a) DC-side current from the GSC. (b) DC-side current from the RSC.

shown in Fig. 8, it can be seen that the back-to-back power converters include the same average dc-side current. However, the harmonic component of the GSC is much lower, as its displacement angle of in-phase or out-of-phase keeps the RMS value to a minimum.

In order to verify the previous analysis, the simulation is carried out at the wind speed of 12 m/s, and the dc-side current from the GSC, the rotor-side converter, and the dc-link current are shown in Fig. 9. Meanwhile, their average values and THD are listed and compared with the theoretical calculations, as shown in Fig. 10. The calculated THD of the dc-side current from the GSC and the rotor-side converter is 38% and 105%,

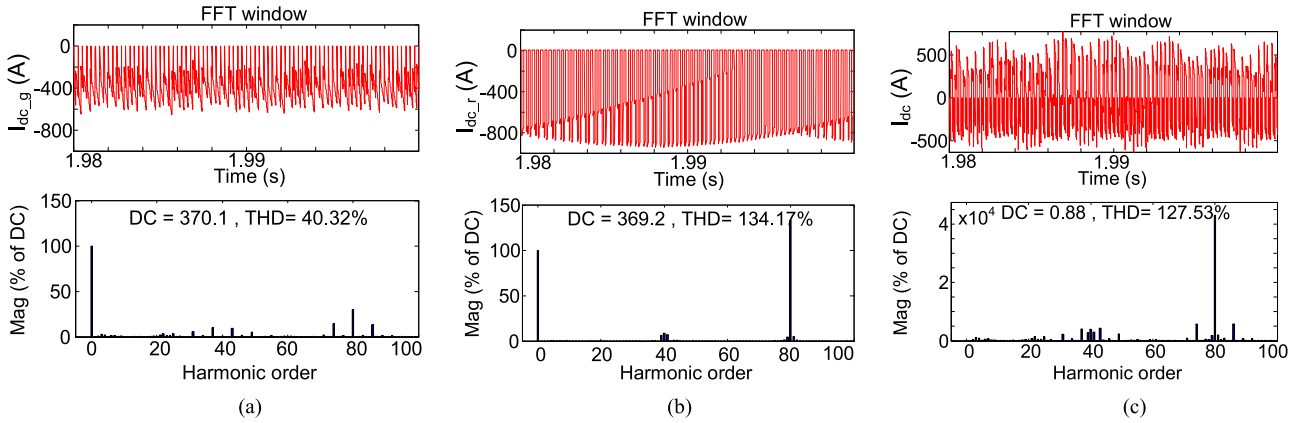

Fig. 9. Simulation result of DC-side current at wind speed of 12 m/s. (a) DC-side current from the GSC. (b) DC-side current from the rotor-side converter. (c) Current of dc-link capacitor.

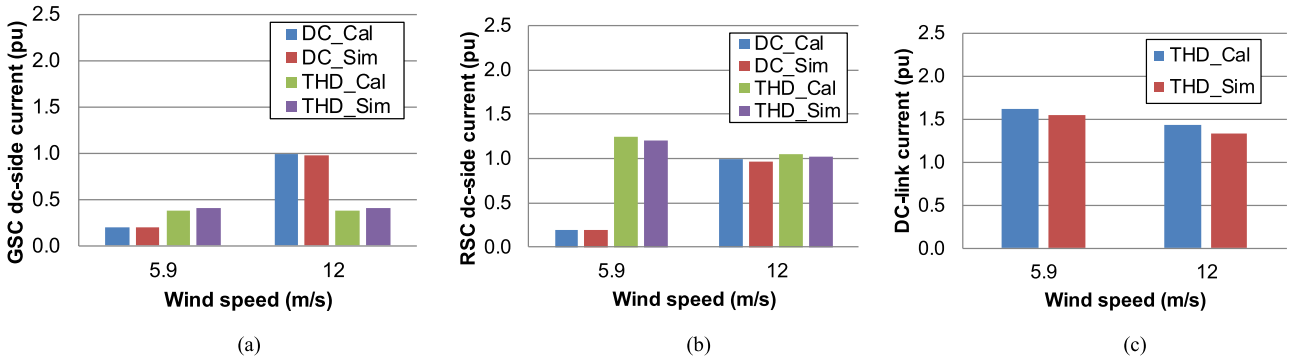

Fig. 10. Harmonic comparison between the calculation (Cal) and simulation (Sim) of dc-link current. (a) DC-side current from the GSC. (b) DC-side current from the RSC. (c) Current of dc-link capacitor.

while their simulated THD is 40% and 134%. It can be seen that the calculated THD is a bit lower due to the assumption of a pure sinusoidal ac-side current. Moreover, the THD of the dc-link current between the calculation and the simulation can be compared. By using the same approach, the comparison is made at the wind speed of 5.9 m/s as well. It can be seen that the calculated THD of the dc-link current matches well the simulation.

C. Capacitor Current Measurement in a Down-Scaled DFIG Setup

In order to verify the electrical stresses of the power capacitors used in the ac-side and dc-side, some experiments are carried out on a down-scaled 7.5 kW DFIG system, whose parameters are listed in Table I. As shown in Fig. 11, the DFIG is dragged by a squirrel-cage motor, the back-to-back power converters are established by using two Danfoss 5.5-kW motor drives. Since each motor drive has its own dc-link capacitor, it can be seen that there are two capacitors $C_{\rm dc1}$ and $C_{\rm dc2}$ referring to the capacitor from the GSC and the rotor-side converter, respectively. The control scheme of both power converters is realized by dSPACE 1006. It is worth noting that the switching frequencies are set to 5 kHz, and the dc-link voltage is regulated to be 650 V.

In order to investigate the different loading conditions impacts on the electrical stresses of the power capacitor, the rotor speeds of 1200, 1500, and 1800 r/min are used to emulate the subsynchronous, synchronous, and super-synchronous modes of the induction generator. In the case of subsynchronous mode, where the rotor speed of the DFIG is maintained at 1200 r/min, it is assumed that 1.5 kW (0.2 pu) active power is provided from the stator-side of the DFIG. The voltage and current of the GSC are measured to observe the operation conditions of the DFIG, while the current flowing through the ac-side and dc-side capacitor is monitored in order to evaluate their electrical stresses. It is noted that the current between the back-to-back power converters is used to indirectly reflect the current of the dc-link capacitor due to the compact dc-link bus bar. As shown in Fig. 12(a), it is evident that the GSC absorbs the active power from the grid due to the positive slip of 0.2. In respect to the ac-side capacitor current, due to the switching frequency of 5 kHz, the dominating harmonics are around 5 and 10 kHz, which agrees well with the theoretical expectation. In addition,

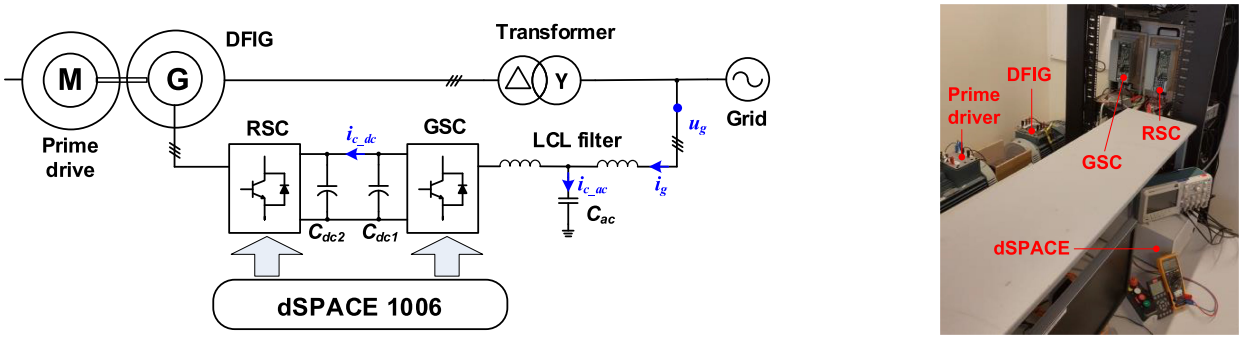

(a) (b)

Fig. 11. 7.5-kW down-scaled DFIG test setup. (a) System configuration. (b) Photo of experimental test rig.

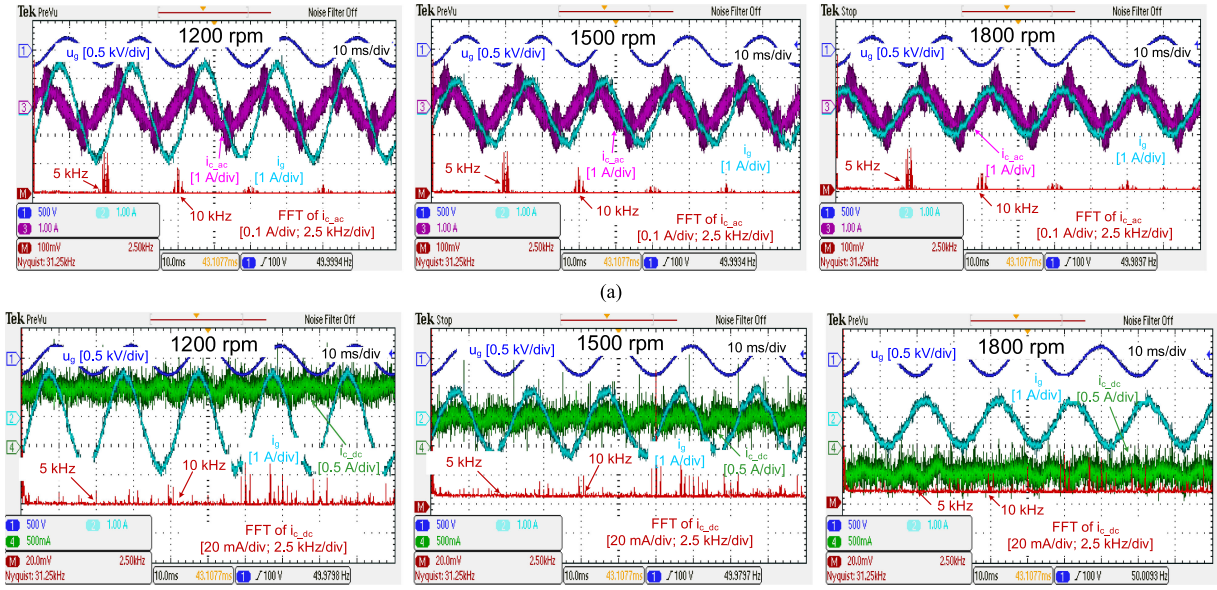

(a)

(b)

Fig. 12. Measured current waveforms of power capacitor at various loading conditions. (a) AC-side capacitor current. (b) DC-side capacitor current.

the current of the dc-link is shown in Fig. 12(b), and it can be seen that the dominating harmonics appear at multiple of the switching frequency.

In the case of the synchronous mode with 0.3 pu active power, the grid-side current is almost the same with the ac-side capacitor current due to no active power flowing through the GSC. At the super-synchronous mode with 0.4 pu active power, as the GSC feeds the active power to the grid because of the negative slip, the grid-side current is in the opposite phase with respect to the power grid, and the dc-side current also become negative. Nevertheless, the dominating harmonics of the ac-side and dc-side capacitors appear at multiple of the switching frequency, which hardly changes regardless of the operation modes.

IV. Lifetime Estimation of Individual Capacitor

In this section, based on the harmonic component of the dc-side and ac-side capacitors, their power losses and thermal behavior can be investigated at typical operation points. Then, the mission profile based thermal stress can be evaluated, which serves to predict the operational lifecycle of the capacitors.

A. Capacitor Lifetime Model

In many applications, the lifetime of electronic devices is directly linked to the lifetime of the capacitors inside. In respect to the Al-CAPs used in the dc-link, the main failure mechanism refers to the electrolyte loss that leads to a drift of the electrical parameters. Generally, there are three dominating factors that determine its lifecycle. Specifically, the ambient temperature and ripple current cause the electrolyte diffusion through the capacitor seal, while the applied voltage induces the electrochemical reaction at the dielectric layer [16]. As a consequence, the lifetime model for the Al-CAP can be expressed as

$$L_x = L_r \cdot 2^{\frac{T_r - T_a}{10}} \cdot 2^{\left(1-\left(\frac{I_x}{I_r}\right)^2\right)\cdot\frac{\Delta T_o}{n_1}} \cdot \left(\frac{V_r}{V_x}\right)^{n_2} \tag{6}$$

TABLE II
CAPACITORS LIFETIME MODEL PARAMETERS AND THEIR LIMITATION

	Value	Comment	Value	Comment
	Al-CAP		MPF-CAP	
Rated lifetime L_r (hour)	6,000		100,000	
Upper categorized temperature T_r (ºC)	105		75	
Rated ripple current I_r (A)	13.4	Measured at 100 Hz; maximum 3 pu	30	Measured at 10 kHz
Rated voltage V_r (V)	400		780	
Core temperature rise at rated ripple current ΔT_o (ºC)	5/10	10 for 105 ºC capacitor; 5 for 85 ºC capacitor	/	
Coefficient of temperature rise n_1	5-10	Vary with ambient temperature [18]	/	
Voltage exponent coefficient n_2	3/5	n_2=3, if 0.5≤V_r/V_x<0.8; n_2=5, if 0.8≤V_r/V_x<1.0	0.7/15/∞	n_2=0.7, if 0.6≤V_r/V_x<1; n_2=15, if 1≤V_r/V_x<1.25; n_2=∞, if 1.25≤V_r/V_x<1.3
ESR (mΩ)	/		3.0	Measured at 10 kHz
Dissipation factor tanδ	/		2e-4	
Thermal resistance from core to ambient (ºC/W)	/		14.1	

where L_x denotes the hours to failure used in the real application, while L_r denotes the hours to the failure of the rated voltage V_r, nominal ripple current I_r, and upper categorized temperature T_r. The first, second, and third components denote the impact from the ambient temperature T_a, applied ripple current I_x and used voltage V_x. The impact from the ambient temperature obeys the Arrhenius law, and a minimum of the 40 °C ambient temperature range is used in order to exactly follow (6) [17]. The amount of ripple current actually affects the core temperature of the capacitor, where ΔT_o denotes the core temperature increase at rated ripple current, and n_1 denotes the acceleration coefficient of temperature rise due to the ripple. Since the core temperature is not easy to be accessed and the thermal resistance is changed with the core temperature, the ripple current can normally be regarded as an indirect core temperature indicator. Moreover, as the equivalent series resistance (ESR) is not fixed at different current harmonic frequencies, the harmonic order of the current needs to be extracted by using the FFT analysis, and each harmonic current causing the same power dissipation needs to be calculated at 100 Hz, which is normally considered in the datasheets. Another factor lies in the applied voltage, and the exponent coefficient n_2 differs with manufacturers. The detailed parameters of the lifetime model for the used Al-CAP are listed in Table II.

Due to the less demanded capacitance, the higher withstand voltage, and the nonpolarity, the film capacitor is normally selected to mitigate the PWM harmonics between the power converter and the grid. As the polypropylene loss becomes the main failure mechanism, it is evident that the rated lifetime of MPF-CAP (100 000 h at 75 °C) is much higher than that of the Al-CAP (6000 h at 105 °C). However, the MPF-CAP is more sensitive to the applied voltage, and the lifetime decreases rapidly with an increasing applied voltage. The relationship between the operational hours and the capacitor core temperature as well as the applied voltage can be expressed as

$$L_x = L_r \cdot 2^{\frac{T_r - T_c}{10}} \cdot \left(\frac{V_r}{V_x}\right)^{n_2} \tag{7}$$

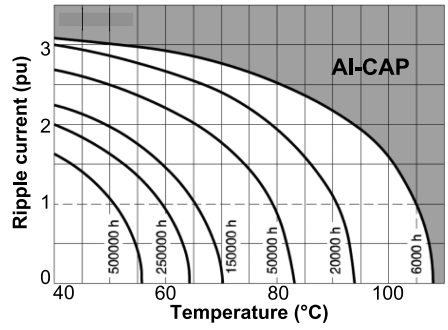

(a)

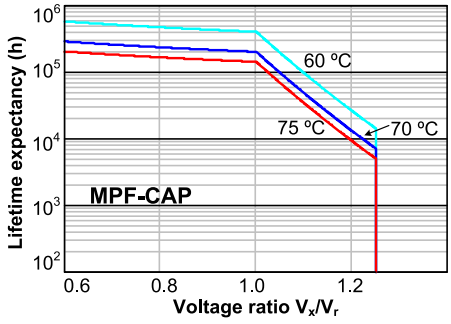

(b)

Fig. 13. Hour to failure with respect to various operating temperatures and applied voltage. (a) Al-CAP [19]. (b) MPF-CAP.

where T_c denotes the core temperature of the film capacitor. It is jointly determined by the ambient temperature, the loss dissipation of the capacitor, and the thermal resistance from the core to the case and the case to the ambient. The detailed parameters for the lifetime model are listed in Table II, which can graphically be described as shown in Fig. 13.

B. Mission Profile-Based Lifetime Estimation

According to the mission profile of the wind turbine system (e.g., wind speed and ambient temperature), the general

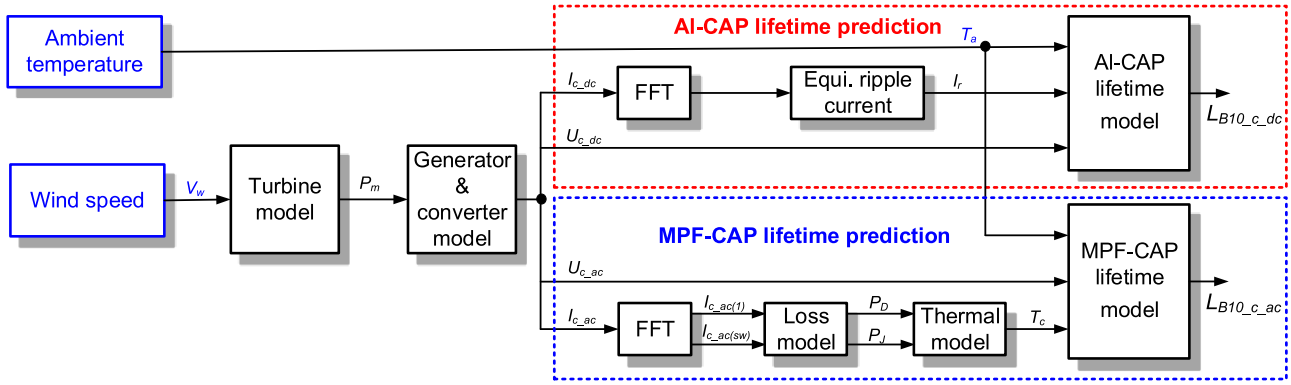

Fig. 14. Flowchart to calculate B_{10} lifetime from mission profile (ambient temperature and wind speed).

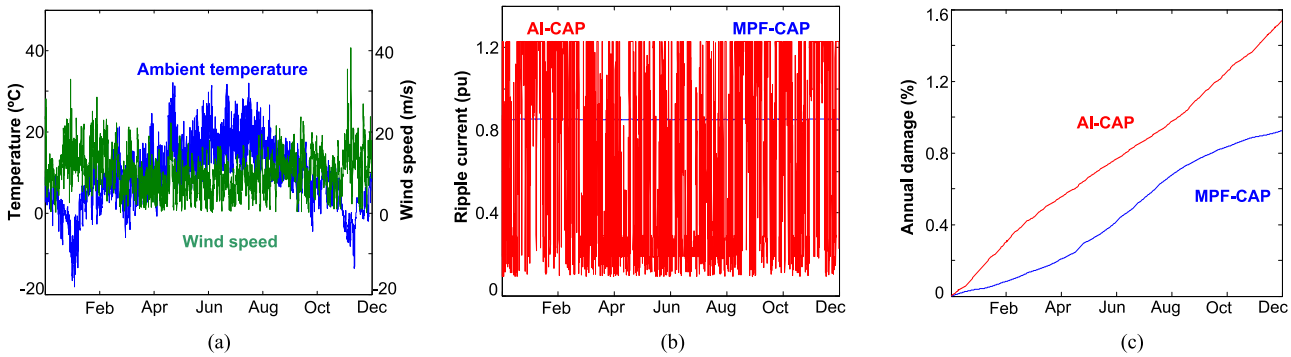

Fig. 15. Annual profile comparison between the MPF-CAP and the Al-CAP. (a) Ambient temperature and wind speed. (b) Ripple current. (c) Accumulated damage.

procedure to calculate the lifetime of the Al-CAP and MPF-CAP is shown in Fig. 14. On the basis of the wind speed, the produced power can be predicted by the MPPT curve, and the current and voltage stresses of each capacitor can be evaluated with the generator and converter models. In respect to the Al-CAP, the ripple current can be calculated with the PWM pattern of power switches in the back-to-back power converters. It is worth mentioning that, considering the ESR curve with the various frequencies, the dominating switching harmonics need to be converted to 100 Hz, which is normally specified in the dc-link capacitor datasheet. Together with the ambient temperature profile, the life expectancy of the Al-CAP can be predicted.

As the lifetime model of the MPF-CAP is tightly related to its core temperature and the applied voltage, the procedure slightly differs with the Al-CAP. Considering both the dielectric loss and the Joule loss dissipation, the core temperature of the capacitor can be jointly decided by the core-ambient thermal resistance and the ambient temperature profile. With the applied voltage calculated by the PWM pattern of the power switch and the characteristics of the *LCL* filter, the lifetime of the MPF-CAP can be estimated.

With the annual wind speed (Class I) and ambient temperature with a sample rate of 1 h, as shown in Fig. 15(a), the ripple current of the Al-CAP and MPF-CAP is shown in Fig. 15(b). As the sample time interval is much higher than the capacitor thermal time constant (typically several minutes), it can roughly be assumed that the core temperature of the capacitor reaches steady-state and stays constant within every sample period. The lifetime damage can thereby be calculated by using the sample period over its corresponding hours to failure calculated in (6) and (7), which is accumulated from a sample period to the whole operational year. As a result, the annual damage of the both types of the capacitors can be deduced and shown in Fig. 15(c), where the lifecycle of the capacitor runs out when the accumulated damage reaches 1. It is worthwhile to mention that the hours to failure is defined as the B_{10} lifetime—only 10% of the samples fails when the operational hours reach this condition. It can be seen that the ripple current of the MPF-CAP is much smoother, as the current harmonic hardly changes with different wind speeds. Moreover, the annual damage of the MPF-CAP is lower due to the fact that it contains much longer rated lifetime (100 000 h) compared to the Al-CAP (6000 h).

V. Time-to-Failure of Capacitor Banks

On the basis of the tested failure data, the B_{10} lifetime of the individual capacitor can be converted into its unreliability curve along with operation hours. Then, the reliability of the capacitor bank can be evaluated with the help of the reliability block diagram.

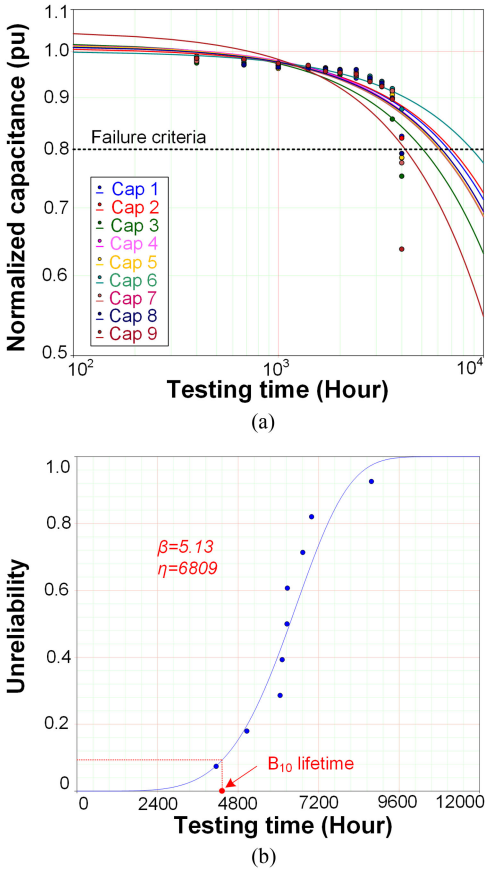

Fig. 16. Degradation results for nine capacitors (Cap 1–Cap 9) at the rated voltage, rated ripple current, and upper operational temperature. (a) Normalized capacitance. (b) Unreliability of capacitors along with operation time by using Weibull distribution.

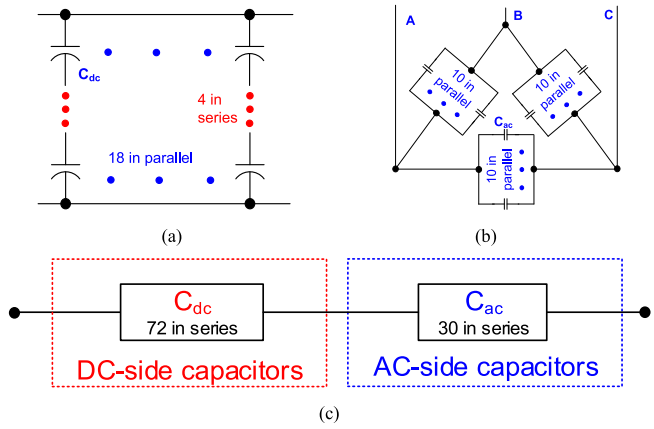

Fig. 17. Configuration of the capacitor banks and equivalent reliability block diagram. (a) DC-side capacitor bank. (b) AC-side capacitor bank. (c) Reliability logics of the whole capacitor bank.

In order to implement the accelerated degradation testing of the capacitor, the testing system is composed of a climatic chamber, a ripple current tester, and an *LCR* meter. Then, a degradation test are performed with a series of nine capacitors (680 μF/63 V) at the rated voltage, rated ripple current, and upper operational temperature, where the normalized capacitance are regularly measured during 4000 testing hours. As shown in Fig. 16(a), the degradation data are analyzed by using the software tool Reliasoft Weibull++. As the reduction rate of the capacitance increases significantly after 80% of its initial values, 20% of capacitance drop is considered as the end-of-life criteria, and the time-to-failure of each capacitor can be estimated. Presented by the Weibull distribution, the unreliability function is fitted in Fig. 16(b) with the shape factor β of 5.13 and the scaling factor η of 6809. It is worthwhile to mention that although the reliability data obtained from the test condition is different with field operation conditions, the electrical–thermal stresses of the capacitor can be regarded equivalent to cause the thermal-related aging and wear-out issues. Specifically, it is believed that the high-order harmonics introduced by the PWM switching can produce the same power losses and thermal stresses as the low-order harmonic in the case that the relationship between the ESR and the frequency is well established.

In order to fulfill the high enough capacitance or withstand the voltage stress, plenty of the capacitors are connected in series or parallel in order to form the capacitor bank. The detailed structure of the dc-side and ac-side capacitor bank is shown in Fig. 17(a) and (b), respectively. Since any failure of the individual capacitor may result in the degraded performance of the capacitor bank, all of the capacitors are connected in series in the reliability block diagram, as shown in Fig. 17(c).

Based on the annual damage of both the MPF-CAP and the Al-CAP, as shown in Fig. 15(c), their B_{10} lifetime can be calculated as 108 and 65 years, respectively. In order to assess the reliability performance for the capacitor bank, the B_{10} lifetime of the individual capacitor is insufficient, and its time-to-failure distribution, which considers the parameter variations and tolerance uncertainties of the capacitor samples, is required in order to apply the reliability block calculation. Since the Weibull shape parameter is identical in the case of the same failure mode [20], the tested value from Fig. 16(b) can again be used, and the whole unreliability curve along with the operational hour can be obtained, as shown in Fig. 18(a) and (b). Moreover, the unreliability curve of the capacitor bank can be deduced from the individual capacitor with the reliability logics as shown in Fig. 17(c). Seen from the 15-year designed lifetime of the capacitor bank, the damage of the individual MPF-CAP becomes 0.0005%, while the MPF-CAP bank damage significantly increases to 0.015%. It is evident that the reliability issue becomes more critical from the single capacitor to the whole capacitor bank, especially when a large amount of the capacitors are applied to form the bank. Similarly, within the 15-year designed lifetime, the damage of the single Al-CAP and the Al-CAP bank reaches 0.0056% and 0.4%, respectively. By using the same approach, the unreliability curve of the whole capacitor bank, which consists of the Al-CAP bank and the MPF-CAP bank, can be calculated as shown in Fig. 18(c). It can be seen that the Al-CAP bank dominates the capacitor bank lifetime. Furthermore, it is noted that the B_1 lifetime of the capacitor bank lasts 18 years, which fulfills the 30-year designed lifecycle of the wind power converter.

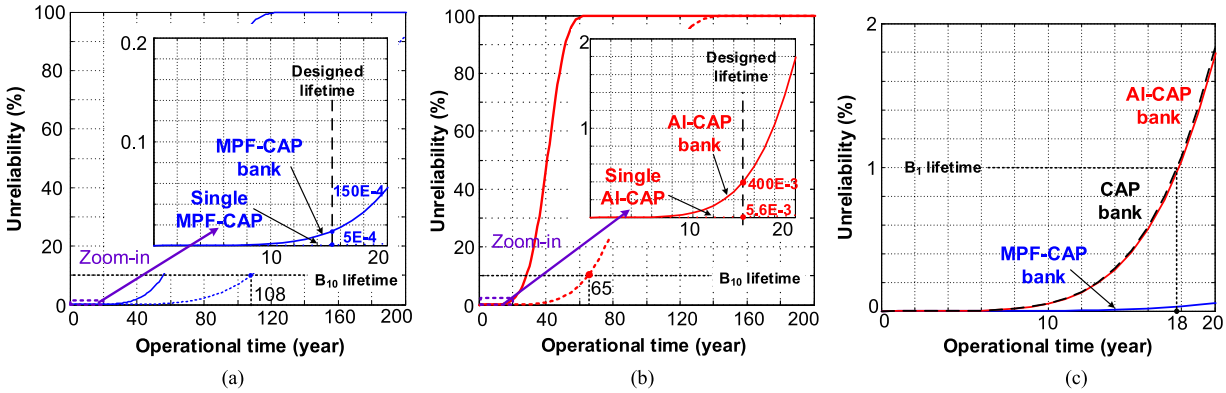

Fig. 18. Unreliability curve from the single capacitor to the capacitor bank. (a) DC-side capacitor bank. (b) AC-side capacitor bank. (c) Whole capacitor bank.

VI. Conclusion

Aiming at the DFIG-based wind power converter, an analytical approach to evaluate the reliability of the power capacitor banks is described in this paper. It starts with the electrical stresses calculation of the ac-side filter capacitor and dc-link capacitor at various loading conditions. The percentile lifetime of the single capacitor can be predicted according to the annual electrothermal profile, which can further be translated into the Weibull function based time-to-failure distribution of the power capacitor by considering the parameter variations.

With the electrical stresses of the power capacitor experimentally verified in the down-scaled 7.5 kW prototype, the reliability curves of the dc-link capacitor bank and the ac-side filter capacitor bank are presented and compared in a 2-MW wind turbine system. It can be seen that the lifecycle is dominated by the dc-link capacitor bank due to its lower rated lifetime of the Al-CAP. It is suggested that the film capacitor may get more involved in the future dc-link solution, due to its reduced cost, improved power density, and longer life expectancy.

References

[1] F. Blaabjerg and K. Ma, "Future on power electronics for wind turbine systems," *IEEE J. Emerg. Sel. Topics Power Electron.*, vol. 1, no. 3, pp. 139–152, Sep. 2013.

[2] H. Polinder, J. A. Ferreira, B. B. Jensen, A. B. Abrahamsen, K. Atallah, and R. A. McMahon, "Trends in wind turbine generator systems," *IEEE J. Emerg. Sel. Topics Power Electron.*, vol. 1, no. 3, pp. 174–185, Sep. 2013.

[3] H. Wang *et al.*, "Transitioning to physics-of-failure as a reliability driver in power electronics," *IEEE J. Emerg. Sel. Topics Power Electron.*, vol. 2, no. 1, pp. 97–114, Mar. 2014.

[4] M. Liserre, R. Cardenas, M. Molinas, and J. Rodriguez, "Overview of multi-MW wind turbines and wind parks," *IEEE Trans. Ind. Electron.*, vol. 58, no. 4, pp. 1081–1095, Apr. 2011.

[5] "ZVEI - Handbook for robustness validation of automotive electrical/electronic modules," Jun. 2013.

[6] K. Ma, M. Liserre, F. Blaabjerg, and T. Kerekes, "Thermal loading and lifetime estimation for power device considering mission profiles in wind power converter," *IEEE Trans. Power Electron.*, vol. 30, no. 2, pp. 590–602, Feb. 2015.

[7] D. Zhou, F. Blaabjerg, M. Lau, and M. Tonnes, "Optimized reactive power flow of DFIG power converters for better reliability performance considering grid codes," *IEEE Trans. Ind. Electron.*, vol. 62, no. 3, pp. 1552–1562, Mar. 2015.

[8] T. Wang and S. Lu, "A comprehensive analysis of DC-link current for single phase H-bridge inverter under harmonic output currents," in *Proc. IEEE Energy Convers. Congr. Expo.*, 2017, pp. 652–658.

[9] H. Jedtberg, M. Langwasser, R. Zhu, G. Buticchi, and M. Liserre, "Impacts of rotor current control targets on DC-link capacitor lifetime in DFIG-based wind turbine during grid voltage unbalance," in *Proc. IEEE Energy Convers. Congr. Expo.*, 2017, pp. 3489–3495.

[10] B. P. McGrath and D. G. Holmes, "A general analytical method for calculating inverter DC-link current harmonics," *IEEE Trans. Ind. Appl.*, vol. 45, no. 5, pp. 1851–1859, Sep. 2009.

[11] X. Pei, W. Zhou, and Y. Kang, "Analysis and calculation of DC-link current and voltage ripples for three-phase inverter with unbalanced load," *IEEE Trans. Power Electron.*, vol. 30, no. 10, pp. 5401–5412, Oct. 2015.

[12] C. Liu, D. Xu, N. Zhu, F. Blaabjerg, and M. Chen, "DC-voltage fluctuation elimination through a DC-capacitor current control for DFIG converters under unbalanced grid voltage conditions," *IEEE Trans. Power Electron.*, vol. 28, no. 7, pp. 3206–3218, Jul. 2013.

[13] M. H. Bierhoff and F. W. Fuchs, "DC-link harmonics of three-phase voltage-source converters influenced by the pulsewidth-modulation strategy—An analysis," *IEEE Trans.Ind. Electron.*, vol. 55, no. 5, pp. 2085–2092, May 2008.

[14] M. Liserre, R. Teodorescu, and F. Blaabjerg, "Stability of photovoltaic and wind turbine grid-connected inverters for a large set of grid impedance values," *IEEE Trans. Power Electron.*, vol. 21, no. 1, pp. 263–272, Jan. 2006.

[15] G. Shen, X. Zhu, J. Zhang, and D. Xu, "A new feedback method for PR current control of LCL-filter-based grid-connected inverter," *IEEE Trans. Ind. Electron.*, vol. 57, no. 6, pp. 2033–2041, Jun. 2010.

[16] Jianghai Appl. Notes, "Electrolytic capacitor lifetime estimation," 2010. [Online]. Available: jianghai-america.com/uploads/technology/JIANGHAI_Elcap_Lifetime_-_Estimation_AAL.pdf

[17] Nippon Chemi-Con Techn. Notes, "Judicious use of aluminum electrolytic capacitors," 2010. [Online]. Available: https://www.chemi-con.co.jp/e/catalog/aluminum.html

[18] Nichicon Appl. Notes, "General descriptions of Aluminum electrolytic capacitors," 2008. [Online]. Available: http://www.nichicon.co.jp/english/products/pdf/aluminum.pdf

[19] TDK Appl. Notes, "Aluminum electrolytic capacitors - general technical information," 2008. [Online]. Available: https://de.tdk.eu/download/185386/5f33d2619fa73419e2a4af562122e90c/pdf-generaltechnicalinformation.pdf

[20] D. Zhou, H. Wang, and F. Blaabjerg, "Lifetime estimation of electrolytic capacitors in a fuel cell power converter at various confidence levels," in *Proc. IEEE 2nd Southern Power Electron. Conf.*, 2016, pp. 1–6.

[21] D. Zhou and F. Blaabjerg, "Reliability evaluation of power capacitors in a wind turbine system," in *Proc. IEEE Appl. Power Electron. Conf.*, 2018, pp. 3264–3269.

[22] D. Zhou, F. Blaabjerg, T. Franke, M. Tonnes, and M. Lau, "Reduced cost of reactive power in doubly fed induction generator wind turbine system with optimized grid filter," *IEEE Trans. Power Electron.*, vol. 30, no. 10, pp. 5581–5590, Oct. 2015.

[23] L. Malesani, L. Rossetto, P. Tenti, and P. Tomasin, "AC/DC/AC PWM converter with reduced energy storage in the DC link," *IEEE Trans. Ind. Appl.*, vol. 31, no. 2, pp. 287–292, Mar. 1995.

[24] M. Liserre, F. Blaabjerg, and S. Hansen, "Design and control of an LCL-filter-based three-phase active rectifier," *IEEE Trans. Ind. Appl.*, vol. 41, no. 5, pp. 1281–1291, Sep. 2005.

[25] "Aluminum can power film capacitors for PFC and AC filter," KEMET datasheet, 2007.
[26] V. H. Prasad, D. Borojevic, and R. Zhang, "Analysis and comparison of space vector modulation schemes for a four-leg voltage source inverter," in *Proc. IEEE Appl. Power Elect. Conf.*, 1997, pp. 864–871.
[27] D. Zhou, F. Blaabjerg, T. Franke, M. Tonnes, and M. Lau, "Comparison of wind power converter reliability with low-speed and medium-speed permanent-magnet synchronous generators," *IEEE Trans. Ind. Electron.*, vol. 62, no. 10, pp. 6575–6584, Oct. 2015.
[28] J. W. Kolar and S. D. Round, "Analytical calculation of the RMS current stress on the DC-link capacitor of voltage-PWM converter systems," *IEE Proc.—Elect. Power Appl.*, vol. 153, no. 4, pp. 535–543, Jul. 2006.
[29] Reliasoft Corporation, "Life data analysis reference," 2016. [Online]. Available: www.reliasoft.com

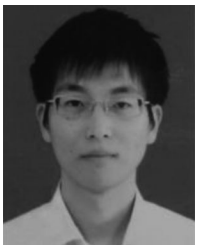

Dao Zhou (S'12–M'15–SM'18) received the B.S. from Beijing Jiaotong University, Beijing, China, in 2007, the M.S. from Zhejiang University, Hangzhou, China, in 2010, and the Ph.D. from Aalborg University, Aalborg, Denmark, in 2014, all in electrical engineering.

Since 2014, he has been with the Department of Energy Technology, Aalborg University, where currently he is an Assistant Professor. His research interests include modeling, control, and reliability of power electronics in renewable energy application.

Dr. Zhou received the Renewable and Sustainable Energy Conversion Systems of the IEEE Industry Applications Society First Prize Paper Award in 2015, and the Best Session Paper at Annual Conference of the IEEE Industrial Electronics Society in Austria in 2013.

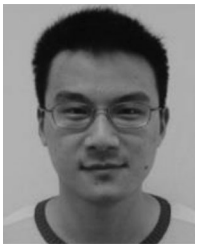

Yipeng Song (M'16) was born in Hangzhou, China. He received the B.Sc. and Ph.D. degrees both from the College of Electrical Engineering, Zhejiang University, Hangzhou, China, in 2010 and 2015, respectvely.

He is currently working as a Postdoc with the Department of Energy Technology, Aalborg University, Aalborg, Denmark. His current research interests include motor control with power electronics devices in renewable-energy conversion, particularly the control, and operation of doubly-fed induction generators for wind power generation.

Yang Liu (M'12–SM'17) was born in Hubei Province, China, in 1979. He received the M.E. and Ph.D. degrees in control science and engineering from the School of Automation, Huazhong University of Science and Technology (HUST), Wuhan, China, in 2005 and 2009, respectively.

He is currently an Associate Professor with the School of Automation, HUST. His research interests include power electronics using SiC and GaN, high-performance ac motor drives, and active harmony filter topology and control.

Frede Blaabjerg (S'86–M'88–SM'97–F'03) received the Ph.D. degree in electrical engineering from Aalborg University, Aalborg, Denmark, in 1995.

From 1987 to 1988, he was with ABB-Scandia, Randers, Denmark. He became an Assistant Professor in 1992, an Associate Professor in 1996, and a Full Professor of power electronics and drives in 1998. Since 2017, he has been a Villum Investigator. He has authored or coauthored more than 500 journal papers in the fields of power electronics and its applications. He is the coauthor of two monographs and editor of six books in power electronics and its applications. His current research interests include power electronics and its applications such as in wind turbines, PV systems, reliability, harmonics, and adjustable speed drives.

Dr. Blaabjerg was the recipient of 24 IEEE Prize Paper Awards, the IEEE PELS Distinguished Service Award in 2009, the EPE-PEMC Council Award in 2010, the IEEE William E. Newell Power Electronics Award 2014, and the Villum Kann Rasmussen Research Award 2014. From 2006 to 2012, he was the Editor-in-Chief for the IEEE TRANSACTIONS ON POWER ELECTRONICS. From 2005 to 2007, he has been a Distinguished Lecturer for the IEEE Power Electronics Society, and from 2010 to 2011, as well as 2017 to 2018, for the IEEE Industry Applications Society. He was nominated in 2014, 2015, 2016, and 2017 by Thomson Reuters to be between the most 250 cited researchers in engineering in the world. In 2017, he became Honoris Causa with the University Politehnica Timisoara, Timişoara, Romania.